ACS OMEGA

http://pubs.acs.org/journal/acsodf

Article

In Situ SAXS and WAXD Investigations of Polyamide 66/Reduced Graphene Oxide Nanocomposites During Uniaxial Deformation

Enyi Chi, Yujing Tang, and Zongbao Wang*

Cite This: *ACS Omega* 2021, 6, 11762−11771

Read Online

ACCESS | Metrics & More | Article Recommendations

ABSTRACT: Epitaxial crystallization between Polyamide 66 (PA66) and reduced graphene oxide (RGO) can enhance the interfacial interaction and the mechanical properties of PA66/RGO nanocomposites. *In situ* two-dimensional synchrotron radiation wide angle X-ray diffraction and small angle X-ray scattering were used to track the structural evolution of the PA66/RGO nanocomposites with an epitaxial crystal during uniaxial deformation. In the PA66/RGO nanocomposites, the structural evolution of non-epitaxial and epitaxial crystals could be clearly analyzed. The non-epitaxial crystal, whose crystal plane can slip, shows the rearrangement and the Brill transition during uniaxial deformation. While the PA66 chains of an epitaxial crystal are held by RGO, the crystal plane could therefore not slip. The epitaxial crystal also constrains the deformation of the amorphous phase and the crystal form transition of non-epitaxial crystals around them. With the content increase of epitaxial crystals, the constraint effect becomes more obvious. Therefore, the rigid epitaxial crystals in the PA66/RGO nanocomposites promote mechanical properties. The present findings can deepen the understanding of structural evolution during the tensile deformation of PA66/RGO nanocomposites and the influence of the epitaxial crystals on the mechanical property in semicrystalline polymers with a H-bond.

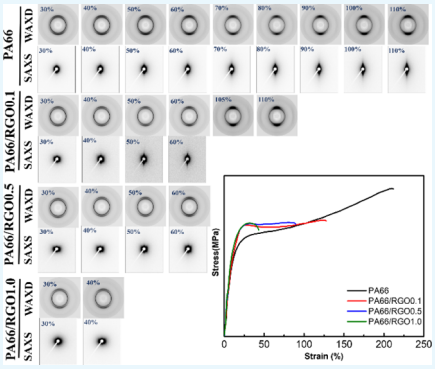

1. INTRODUCTION

Polymer nanocomposites, especially polymer−inorganic nanocomposites, have attracted considerable attention on account of their excellent mechanical properties and function in recent years.[1−4] The interfacial interactions between inorganic nanomaterials and polymers are the most important factor for the high-performance polymer−inorganic nanocomposite.[5−7] In past decades, surface modification of the nanomaterial,[8−11] modification of the polymer,[12] preparing polymer composites via an *in situ* polymerization method,[13−15] and adding a compatibilizer[16,17] as effective methods were developed to enhance the interfacial interactions. The epitaxial crystallization, which is a kind of surface-induced crystallization,[18] can effectively enhance the interfacial interaction and avoid the destruction of polymer−inorganic nanocomposites.[19−24] Epitaxy is generally defined as the growth of one phase on the surface of another phase in one or more strictly defined crystallographic orientation, and the orientation is explained by two-dimensional (2D) or one-dimensional (1D) structural analogy in the plane of contact of the two species.[25] Pashley indicated that 10−15% disregistries of lattice matching were the upper limit of epitaxy.[26] There is also another surface-induced crystallization referred to as graphoepitaxy that is based on surface topology of the substrate as indicated by the crystallization of poly(L-lactic acid) on polyethylene and polypropylene substrates.[27−29]

The 2D reduced graphene oxide (RGO) is an excellent nanofiller because of its periodic structure and excellent properties.[26,30−33] Compared to graphene, RGO possesses better dispersibility in polymers because it has a small amount of oxygen atoms. Hence, RGO has a great potential for improving the mechanical properties of polymers and a lot of polymer/RGO nanocomposites have been studied.[21,22,33,34] Polyamide 66 (PA66), the earliest engineering plastic, is widely used due to its excellent properties.[35−38] PA66 and its nanocomposites are continuously studied.[36−38] As one kind of a typical semicrystalline polymer, PA66 possesses a lot of hydrophilic groups. The determining factor for the crystal structures of PA66 is the ability to form H-bonds between the NH group and the CO group.[39] There are a large amount of H-bonds in the crystalline and amorphous phase of PA66. 20% H-bonds still exist even in the molten state.[39−41] In the injection molding progress of PA66, the α-form crystal is the main crystal form in which the PA66 chains are in the full extended planar zig-zag conformation and are parallel to the *c*-

Received: March 14, 2021
Accepted: April 12, 2021
Published: April 22, 2021

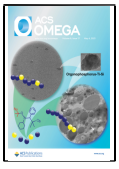

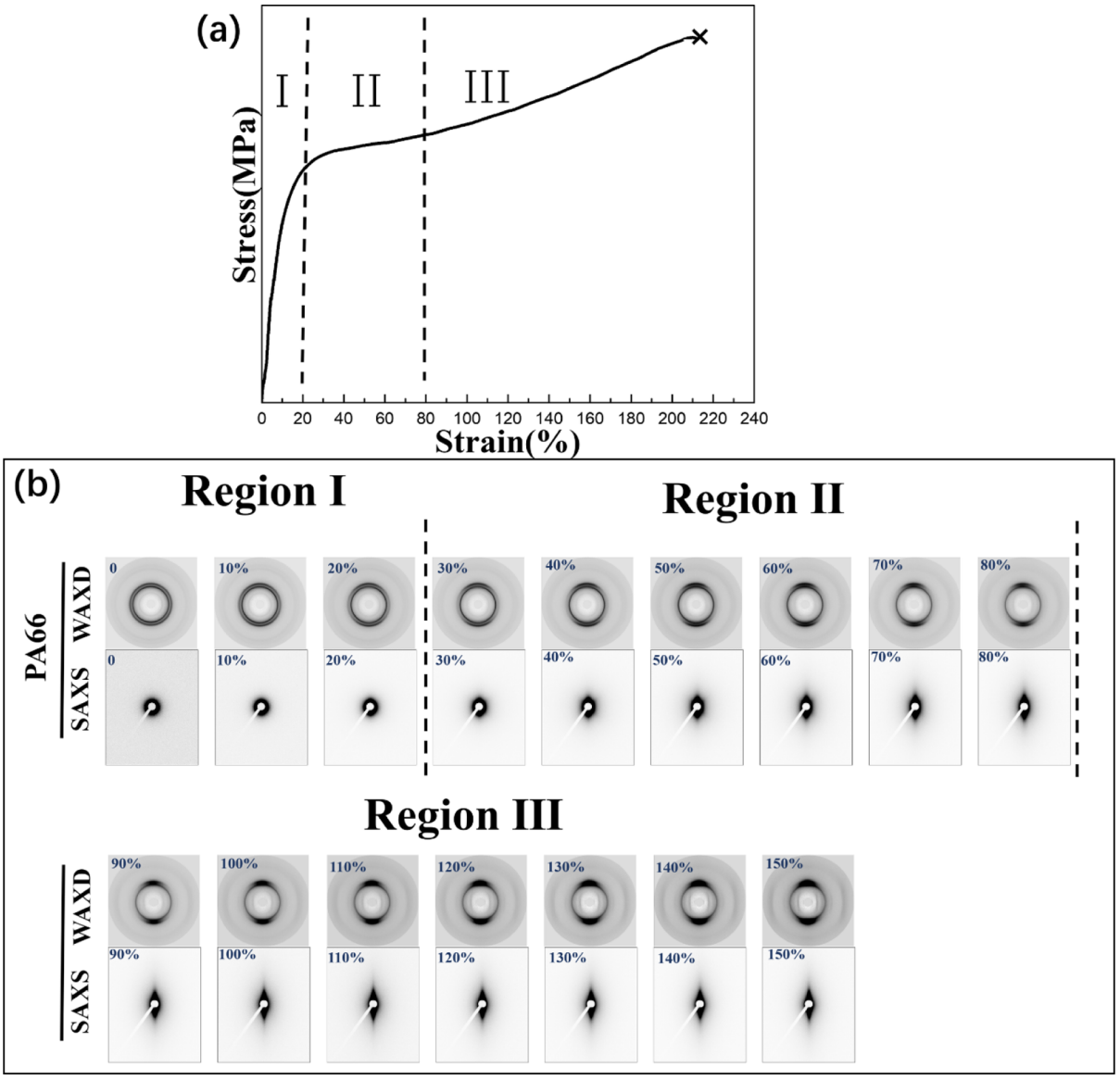

Figure 1. Engineering stress−strain curve (a) together with SAXS/WAXD patterns (b) of pure PA66. Stretching direction is horizontal.

axis direction. The lattice constants of triclinic α-form are a = 0.49 nm, b = 0.54 nm, c = 1.72 nm, α = 48°, β = 77°, and γ = 63°.[35] The other stable crystal form of PA66 is the γ-form crystal (a = 0.49 nm, b = 0.59 nm, c = 1.65 nm, α = 56°, β = 81°, and γ = 60°) which is a pseudohexagonal crystal and the chain axis of γ-form crystal is shorter than the α-form.[42] The crystallographic parameter of the most important periodic structure-⟨2100⟩ RGO spacing (s) is 0.246 nm.[43] Hence, the disregistry (δ) between the c-axis of the α-form PA66 crystal and the crystallographic parameter of ⟨2100⟩ RGO spacing is only 0.1% (δ = 7s − c/c). The α-form crystal, other than the γ-form crystal, of PA66 can epitaxially grow on the surface of laminated RGO in theory. Therefore, PA66 was also a representative of semicrystallinity polymer with H-bonds to investigate the effect of an epitaxial crystal in semicrystallinity polymer/RGO nanocomposites.[44]

In our previous paper,[20] we have studied the structure and mechanical properties of the PA66/RGO nanocomposite. Because of the existence of H-bonds, RGO more easily absorbs the chains of hydrophilic PA66. The PA66 chains can epitaxially crystallize in its α-form on the surface of laminated RGO. The different PA66/RGO nanocomposites showed different mechanical properties owing to different contents of epitaxial crystals. However, the mechanism of enhancing the mechanical properties is rather elusive and should be investigated in depth. Mechanical properties of semicrystalline polymer materials are associated with their deformation behavior and the corresponding structural evolution, and thus the mechanism of deformation behavior plays an important role on the relevant mechanical performances.[45−47] The study of structural development and evolution during the tensile deformation process of semicrystalline polymers cannot only elucidate the deformation mechanism but also enable us to deepen the understanding on the improvement of the mechanical properties of polymer−inorganic nanocomposites. Therefore, the change of structure during deformation should be further studied by the *in situ* method in the PA66/RGO nanocomposite stretching process.

Synchrotron radiation small angle X-ray scattering (SAXS) and wide angle X-ray diffraction (WAXD) are powerful tools to monitor the real-time structural evolution during the deformation process of polymers. They have been widely

https://doi.org/10.1021/acsomega.1c01365
ACS Omega 2021, 6, 11762−11771

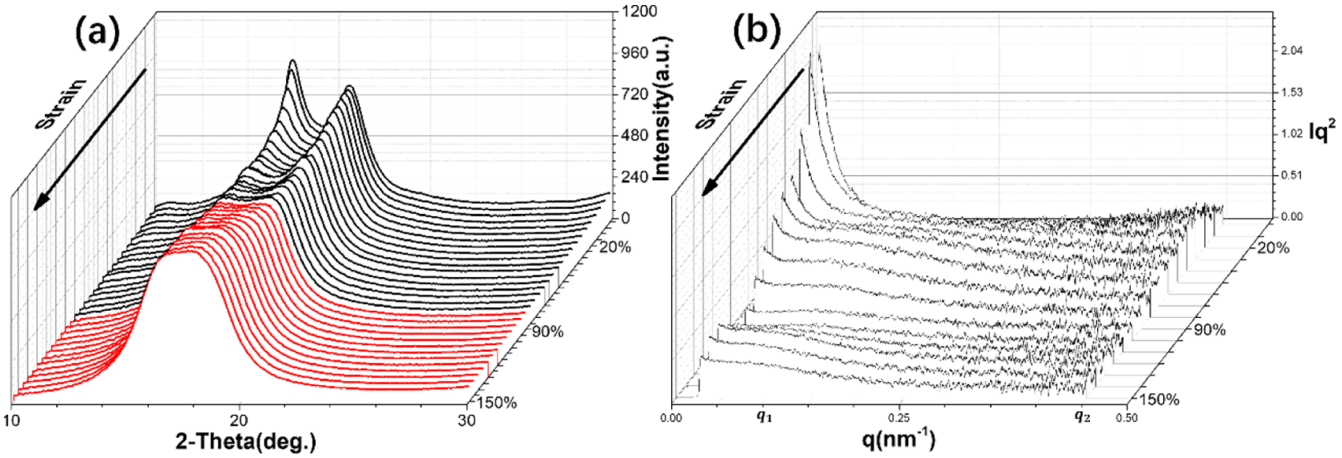

Figure 2. 1D-WAXD curves (a) and Lorentz-corrected SAXS curves (b) of pure PA66 during deformation. The strain increases along the black arrow.

used in the *in situ* examination of structural changes of polymer materials, and the application of synchrotron radiation has dramatically promoted the structural research of semicrystalline polymers.[48−52] *In situ* SAXS can demonstrate the continuous change of periodic structures. By an *in situ* WAXD experiment, the continuous change of crystal forms and orientation degrees can be studied. The cold stretching has been widely accepted for the study on structural evolution and mechanical property of a semicrystalline polymer.[51−54] Although an extensive number and variety of investigations have been carried out on the deformation behavior of semicrystalline polymers, there are few literature studies concerning the tensile deformation behavior of polymer/nanofillers composites, especially for those with epitaxial crystals. We recently reported that strain-induced melting−recrystallization took place in the stretching process of poly(ε-caprolactone) (PCL)/RGO nanocomposites with a low velocity at room temperature, and epitaxial crystallization imposed a restriction effect on the structural transformation of PCL and confirmed that the epitaxial crystallization of PCL upon RGO surfaces is the major factor for the improvement of mechanical properties of PCL/RGO nanocomposites.[54] We also reported that the RGO and HDPE crystals epitaxially grown on the RGO lead to the delay of the structural evolution and then the enhancement of mechanical properties of HDPE/RGO nanocomposites.[55]

Our previous work showed that the crystal of PA66/RGO nanocomposites included the non-epitaxial and the epitaxial crystals, and the content of two kinds of crystal changed, from all non-epitaxial crystals to almost all epitaxial crystals, with the RGO content in nanocomposites.[20] Compared with other systems of polymer nanocomposites with epitaxial crystallization, the structural evolution of non-epitaxial and epitaxial crystals can be easily distinguished in PA66/RGO nanocomposites; therefore, it is an ideal nanocomposite to study the effect of epitaxial crystallization on mechanical properties. In ex situ experiments, the size and type of crystals can be analyzed, but the effect of epitaxial crystals and the structure evolution of polymer crystals are only conjectured. With *in situ* SAXS and *in situ* WAXS measurements, the structural evolution of PA66/RGO nanocomposites with different contents of epitaxial crystals during uniaxial deformation will be systematically investigated in this paper. It is highly expected that an in situ study on the structural evolution during tensile deformation of PA66/RGO nanocomposites with epitaxial crystallization can also deepen the understanding upon the mechanism of nanofillers imposing on the mechanical performance of polymer matrixes.

2. RESULTS AND DISCUSSION

2.1. Structural Evolution of Non-Epitaxial Crystals during Uniaxial Deformation. In a pure PA66 sample, all crystallites are non-epitaxial, so the structural evolution of non-epitaxial crystals and amorphous phase can be observed and analyzed during the stretching process. The stretching processes of pure PA66 and PA66/RGO nanocomposites in the following section can be divided into three stages, namely, the elastic deformation stage (stage I), the plastic deformation stage (stage II), and the strain-hardening stage (stage III), and the patterns of 2D SAXS and 2D WAXD are listed in the corresponding stage.

The stage I contains the strain of 0−20% in the stretching process, as shown in Figure 1. From the patterns of 2D WAXD, the diffraction rings from inner to outward are designated to the (100) and (010) + (110) crystal planes of PA66 triclinic crystals, respectively.[31] As can be seen in Figure 2a, the positions of diffraction peaks of (100) and (010) + (110) lattice planes do not change in the 1D WAXD curves, indicating that the crystal form of PA66 is maintained during the elastic deformation process. However, the diffraction ring of the (010) + (110) lattice plane, which is the outer diffraction ring on the 2D WAXD patterns, changes to the nonuniform cycle because the diffraction signal of meridian direction is stronger than the equatorial direction, implying that the crystal degree of orientation of the pure PA66 sample increases. In Figure 1, the 2D SAXS signal changing from circular to elliptic confirms the increase of crystallite orientation in the stage I. The Lorentz-corrected 1D SAXS curves of pure PA66 only have one slight peak located at the q_2 position (q_2 peak) throughout the stage I (Figure 2b), which accords with our previous work which indicated that the scattering peak of the pure PA66 sample is at q = 0.80 nm^{-1}.[20] Although we only obtain the partial q_2 peak, its variation trend can be distinguished. With the increase of strain, the peak intensity of the q_2 position continually slightly increases and the q_2 peak slightly moves toward a lower q value. The results imply that the stretching of the amorphous phase brings about the increase of the period structure in the stage I. Therefore,

https://doi.org/10.1021/acsomega.1c01365
ACS Omega 2021, 6, 11762−11771

the change of SAXS and WAXD signals is ascribed to the deformation of the amorphous phase and the partial rearrangement of the crystals during the elastic deformation process.

In stage II with a strain of 20−90%, the diffraction peak of the (010) + (110) lattice plane changes from the nonuniform cycle to two semi-arcs (Figure 1), which indicates the increase of the crystal degree of orientation. As can be seen in Figure 2a, the constant positions of diffraction peaks indicate that the crystal form of PA66 is maintained during the plastic deformation process. However, the diffraction peaks of (100) and (010) + (110) lattice planes continuously widen in stage II, which accords with the slight distortion of the PA66 crystals during the stretching. When the strain increases from 20 to 60%, the SAXS signal changes from ellipse to truncated rhombus. When the strain achieves 90%, the truncated rhombus SAXS signal turns into a rhombus. The variation of SAXS signals embodies the rearrangement of crystals. The stress drives the crystals continuously to rearrange along the stretching direction. The truncated rhombus signal indicates that the continuous stretching of the amorphous phase causes the nonoriented crystals to deflect toward the stretching direction. When the truncated rhombus signal turns into a rhombus, the crystals absolutely rearrange along the direction of stress. In the 1D Lorentz-corrected SAXS curves of stage II (Figure 2b), the q_2 peak gradually disappears and the q_1 peak appears. The abovementioned results indicate that the crystals rearrange, the degree of orientation increases, and the size of period structure increases during the plastic deformation process.

The stage III contains the strain of 90−210% in the stretching process, as shown in Figure 1. The 2D WAXD signals of the (010) + (110) lattice plane change from two semi-arcs to two short arcs, indicating that the crystal degree of orientation continuously increases with the strain. As can be seen in Figure 2a, the two peaks of 1D WAXD curves in the stage III (2θ = 16.3 and 19.0°) merge into one peak (2θ = 17.4°), indicating the change of crystal forms, which is also known as the Brill transition.[53] In the merging process of WAXD peaks, the (010) crystal plane of triclinic α-form PA66 crystals slips during the stretching, and ultimately, the crystal form changes from triclinic α-form to pseudo-hexagonal γ-form. From the 2D SAXS patterns in Figure 1, we can clearly observe that the signal similar to a shish crystal appears along the stretching direction. It is well known that crazing and void widely exist in the strain hardening process. As can be seen in Figure 2b, the intensity of the q_1 peak gets weak when the strain is 90−120%. When the strain is greater than 120%, the intensity the of q_1 peak immediately increases. It indicates that the formation and tensioning of voids accompany the transformation of crystal forms in the stage III. The increscence of γ-form crystals and the tensioning of voids are the reason of the enhancement of streak signals.

2.2. Structural Evolution of Epitaxial Crystals during Uniaxial Deformation. It is a fact that the polymer/RGO nanocomposites containing only epitaxial crystals are most impossible. However, we can try to reduce the infection of non-epitaxial crystals. In our previous work, we have obtained the PA66/RGO1.0 nanocomposite containing more epitaxial crystals and few non-epitaxial crystals.[20] Therefore, we study the structural evolution of epitaxial crystals in the PA66/RGO1.0 nanocomposite during uniaxial deformation in this section. As shown in Figure 3, the PA66/RGO1.0 nanocomposite breaks when the strain is about 50%. Therefore, the stretching process only contains the stage I (the elastic deformation stage) and the stage II (plastic deformation stage).

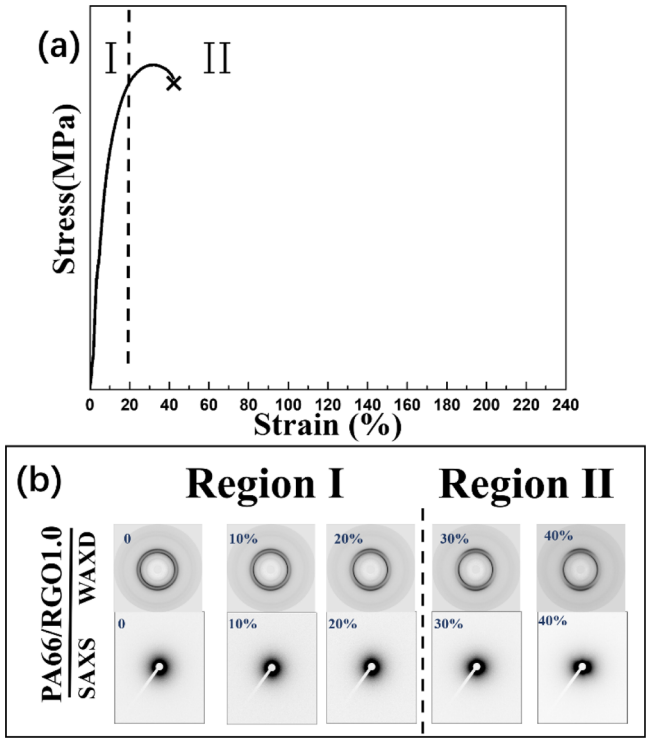

Figure 3. Engineering stress−strain curve (a) together with SAXS/WAXD patterns (b) of PA66/RGO1.0. Stretching direction is along horizontal direction.

We can observe that the change of the PA66/RGO1.0 nanocomposite sample is similar to the pure PA66 sample in the stage I. Because of the addition of RGO, the unstretched sample possesses orientation.[20] As can be seen in Figure 3, the nonuniform diffraction ring of the (010) + (110) lattice plane becomes more focused and the elliptic 2D SAXS signal is stretched during the stretching process. In Figure 4a, the positions of WAXD peaks do not change, indicating that the crystal form of PA66 is maintained during the elastic deformation process. In Figure 4b, there is only q_1 SAXS peak during the stage I, and the position of the q_1 peak does not change and the intensity of the q_1 peak is decreased. In our previous work, it has been proven that the q_1 peak in the unstretched sample is related to the periodic structure of epitaxial crystals.[20] The lack of the q_2 peak indicates that non-epitaxial crystals are seldom. Because the size of epitaxial crystals is large compared to non-epitaxial crystals and the crystal plane of epitaxial crystal is hard to slip, the change of the q_1 peak intensity is ascribed to the voids formed during stretching process. In the stage I, the change of SAXS and WAXD signals originates from the stretching of the amorphous phase.

In the end of the elastic deformation stage, the sample enters the stage II. We can observe the 2D signal change of the stage II with the increase of strain in Figure 3. The 2D diffraction signal changes from a nonuniform cycle to arcs, and the 2D SAXS signal changes from elliptic to a butterfly-like pattern. The change of signals indicates that the degree of orientation is enhanced in the stage II. In Figure 4a, the positions of

https://doi.org/10.1021/acsomega.1c01365
ACS Omega 2021, 6, 11762−11771

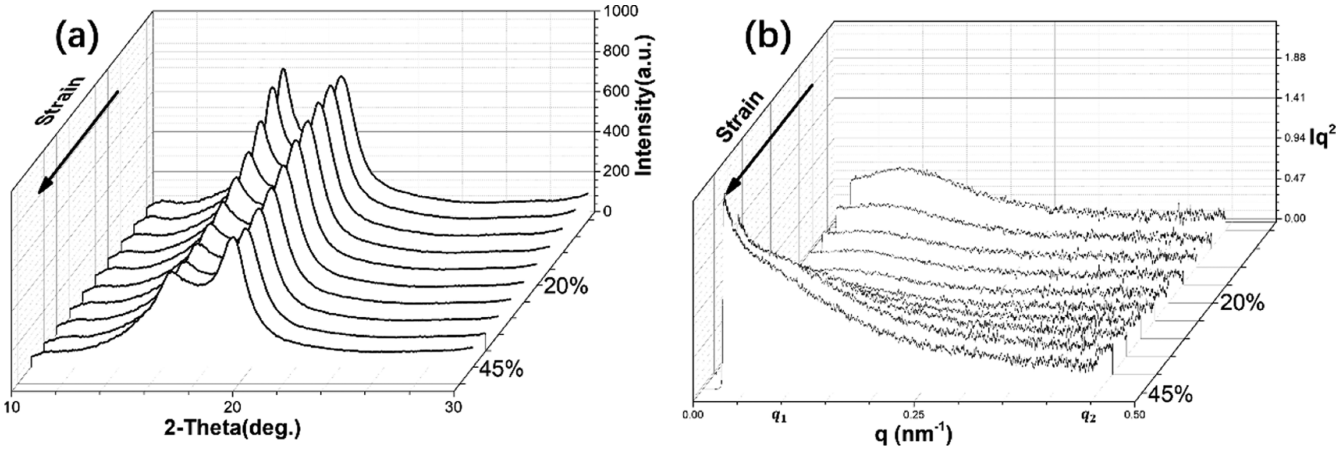

Figure 4. 1D-WAXD curves (a) and Lorentz-corrected SAXS curves (b) of PA66/RGO1.0. The strain increases along the black arrow.

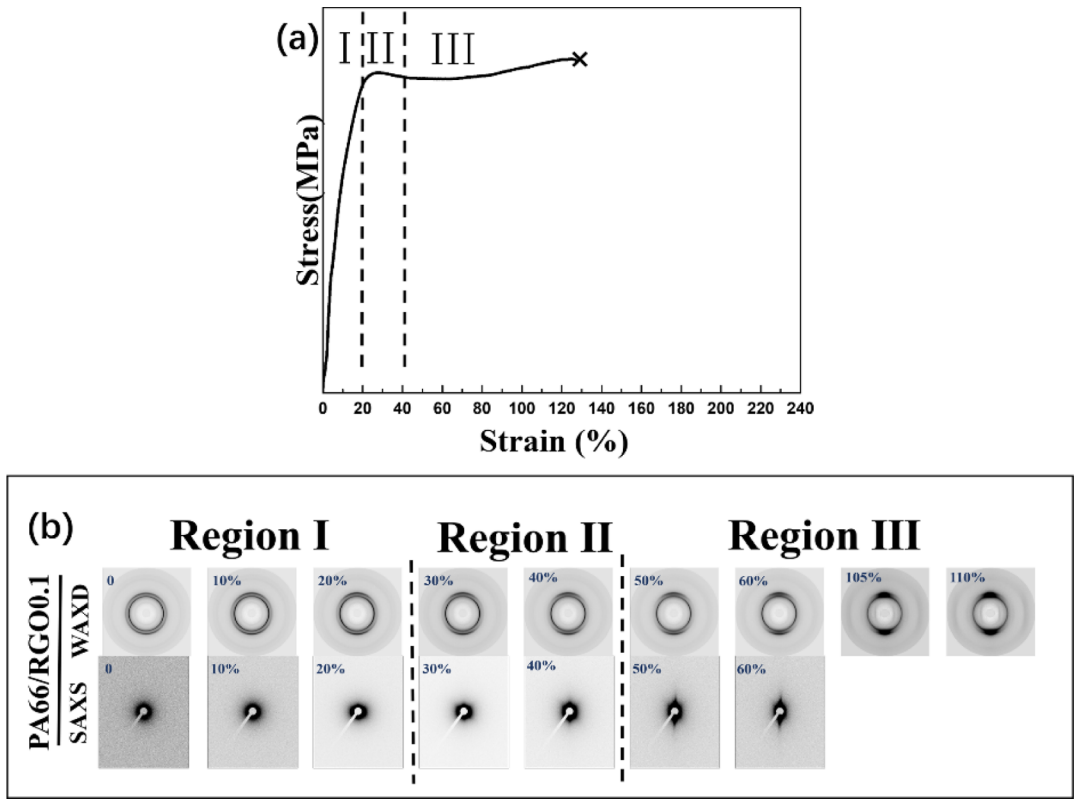

Figure 5. Engineering stress−strain curve (a) together with SAXS/WAXD patterns (b) of PA66/RGO 0.1. Stretching direction is along horizontal direction.

diffraction peaks (2θ = 16.3 and 19.0°) do not change during the stretching process. Hence, the crystal form, in PA66/RGO1.0 nanocomposites, does not change during the stretching process. The change of 1D SAXS curves of the stage II is different from pure PA66. In Figure 4b, we can observe that the q_1 peak is distinct and the position of the q_1 peak remains unchanged. However, the intensity of the q_1 peak first decreases and then increases. The (100) lattice plane is parallel to the surface of RGO when the PA66 crystal epitaxially grows on the surface of RGO. In the α-form crystal of PA66, the PA66 chains are in the fully extended planar zig-zag conformation and parallel to the c-axis direction. Therefore, the epitaxial crystal with α-form is very stable and it is hard to deform and slip. It is the reason that the diffraction peaks and the SAXS peak, except for the intensity, remain unchanged, as shown in Figure 4. Moreover, the mobility of non-epitaxial crystals and amorphous phase is constrained by epitaxial crystals.

2.3. Structural Evolution of Coexisted Epitaxial and Non-Epitaxial Crystals during Uniaxial Deformation. We have discussed the structural evolution of epitaxial crystal and non-epitaxial crystal during uniaxial deformation, respectively. The results of epitaxial crystal and non-epitaxial crystal can help us to more clearly analyze the structural evolution of coexisting epitaxial and non-epitaxial crystals during uniaxial deformation. The PA66/RGO 0.1 and PA66/RGO 0.5 nanocomposites can be the representative of samples with coexisting epitaxial and non-epitaxial crystals.

https://doi.org/10.1021/acsomega.1c01365
ACS Omega 2021, 6, 11762−11771

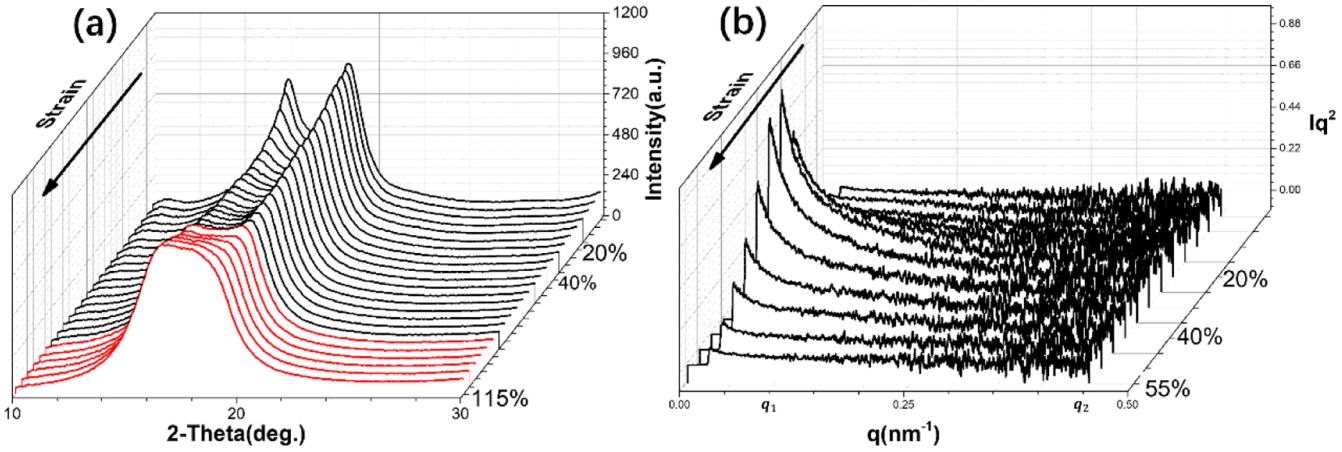

Figure 6. 1D-WAXD curves (a) and Lorentz-corrected SAXS curves (b) of PA66/RGO 0.1 during deformation. The strain increases along the black arrow.

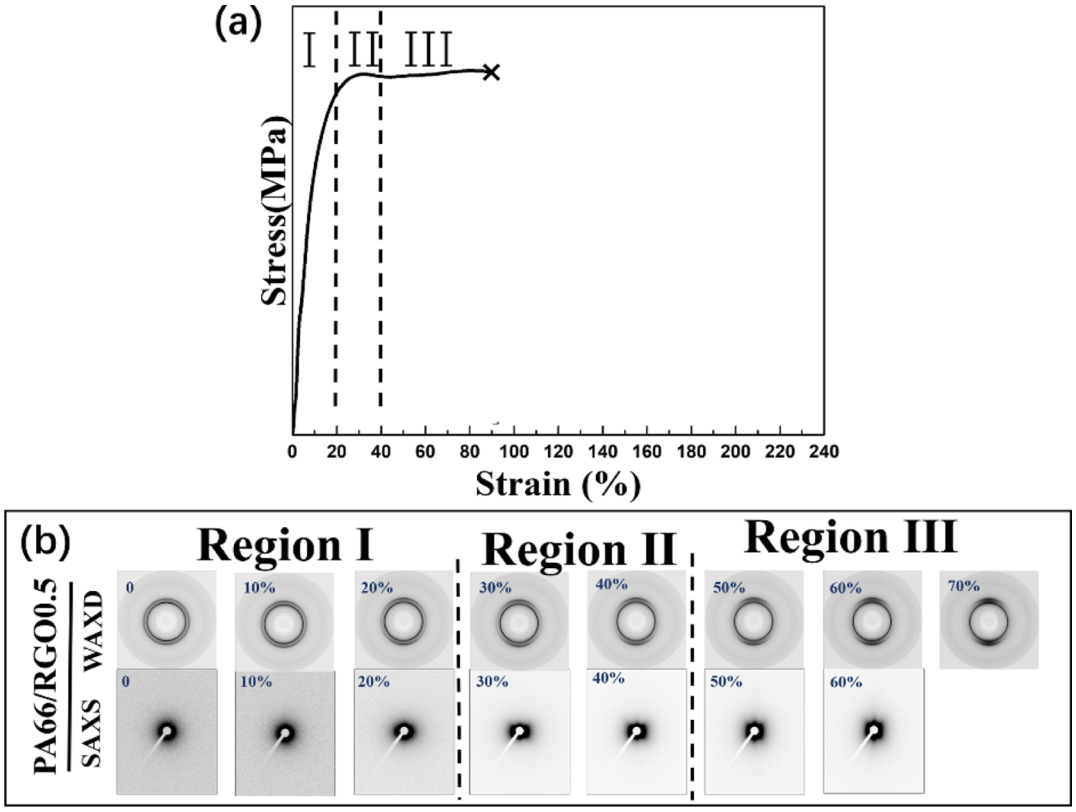

Figure 7. Engineering stress−strain curve (a) together with SAXS/WAXD patterns (b) of PA66/RGO 0.5. Stretching is along horizontal direction.

The signals of WAXD and SAXS and the stress−strain curves are shown in Figure 5 during the uniaxial deformation of PA66/RGO 0.1 nanocomposites. The draw ratio of PA66/RGO 0.1 nanocomposites is between pure PA66 and PA66/RGO 1.0 nanocomposites. The WAXD signals changing from the non-uniform cycle to two arcs during uniaxial deformation indicates that the crystal degree of orientation is enhanced. In Figure 6a, the two diffraction peaks of the 1D WAXD curve (2θ = 16.3 and 19.0°) gradually merge into one. This is consistent with the result of non-epitaxial crystals in a pure PA66 sample. It indicates that the non-epitaxial crystals in the PA66/RGO 0.1 nanocomposites are in the Brill transition process just before the end of the stretching process. The SAXS signals are the superposition signals of epitaxial crystals and non-epitaxial crystals in different stages. The butterfly-like signal appears in the stage II. During the plastic deformation process, the stress drives the crystals continuously to rearrange along the stretching direction. The deformed amorphous phase kept pulling the epitaxial and non-epitaxial crystals. Before the crystal form changes, the crystals were pulled along the direction of deformation. The nonoriented crystals deflect toward the stretching direction, so the degree of orientation increases during the plastic deformation process. The SAXS signal of stage III shows the fusiform shape, and the signal similar to a microcolumnar gap appears in the direction of meridian. We can observe that there is not a SAXS peak in the whole process, as shown in Figure 6b, but the change of the SAXS signal can be distinguished. In the stage II, a new peak

https://doi.org/10.1021/acsomega.1c01365
ACS Omega 2021, 6, 11762−11771

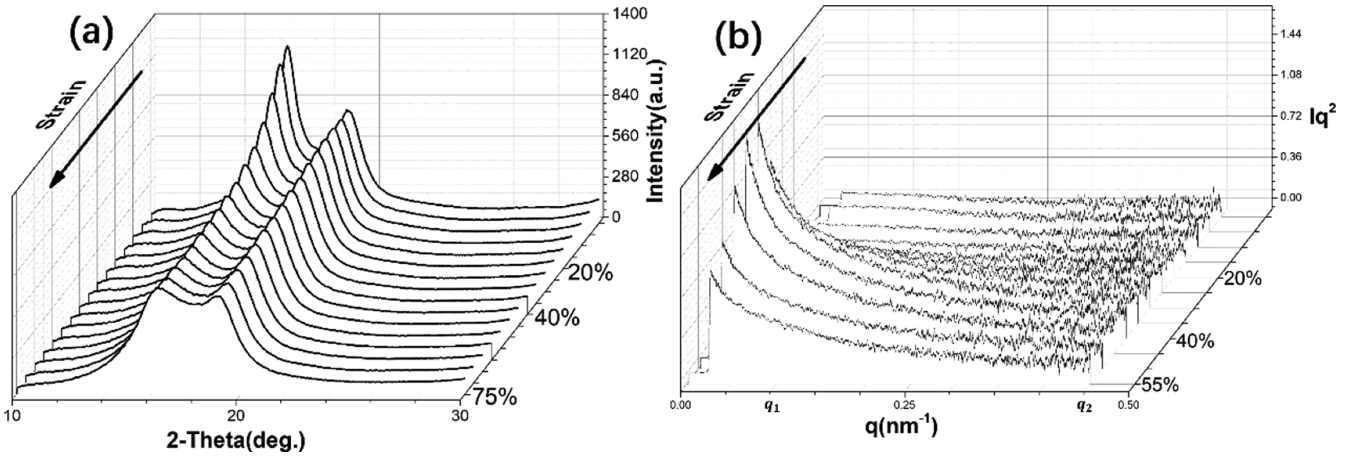

Figure 8. 1D-WAXD curves (a) and Lorentz-corrected SAXS curves (b) of pure PA66/RGO 0.5. The strain increases along the black arrow.

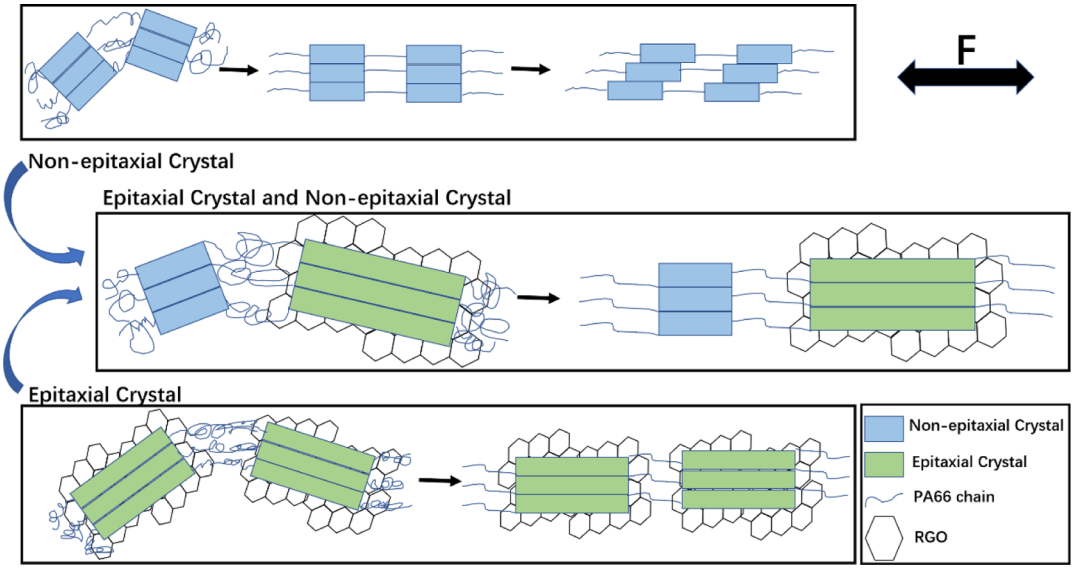

Figure 9. Schematic diagram of structural evolution of non-epitaxial and epitaxial crystals during uniaxial deformation.

begins to emerge near the q_1 position. With the increase of the strain, the peak gradually moves to 0. It indicates that the new periodic structure is formed during the stretching process. It is consistent with the result of WAXD of the slip of crystal plane and the change of the crystal form. In stage III, continuous stretch makes the new peak gradually move to low q and it cannot be detected.

In the stretching process of PA66/RGO 0.5 nanocomposites, the strain is only 90%. However, we can still observe that the stress−strain curve possesses three stages in Figure 7. The WAXD signals change from the non-uniform cycle to two arcs during the stretch process. The result of 1D WAXD of PA66/RGO 0.5 nanocomposites is different from that of PA66/RGO 0.1 nanocomposites. In Figure 8a, the double peaks (2θ = 16.3 and 19.0°) can be observed in the entire stretching process. It is close to the result of PA66/RGO 1.0 nanocomposites. The crystal form does not change in the PA66/RGO 0.5 nanocomposites. The change of SAXS signals is the same as the signals of PA66/RGO 1.0 nanocomposites. In the stretching process, the SAXS signals of the stage I and the stage II and III, respectively, show an ellipse signal and a butterfly-like signal. Figure 8b shows the Lorentz-corrected SAXS curves. In stages I and II, there is no new peak. Until stage III, an obvious peak appears and moves toward q = 0. Because a certain amount of non-epitaxial crystals exist in PA66/RGO 0.5 nanocomposites, the new peak can be assigned to the crystal plane slip of non-epitaxial crystals.

It is obvious that the structural evolution of PA66/RGO nanocomposites should be closely linked to the content of epitaxial crystals during uniaxial deformation. We review the results of pure PA66 and PA66/RGO 1.0: (1) the non-epitaxial crystals rearrange along the tensile direction; (2) non-epitaxial crystals exhibit a crystal-form transition process but epitaxial crystals do not. In other words, RGO constrains the crystal-plane slip of epitaxial crystals. Different contents of RGO lead to a different concentration of epitaxial crystals existing in the PA66/RGO nanocomposites. The structural evolution of PA66/RGO 0.1 is similar to pure PA66, while the structural evolution of PA66/RGO 0.5 is similar to PA66/RGO 1.0. From experimental results, we can easily find that not all of nanocomposites exhibit a crystal-form transition from the α form to γ form during uniaxial deformation. When a small amount of epitaxial crystals exist in the PA66/RGO nanocomposites, the crystals rearrange along the stretching direction and non-epitaxial crystals exhibit the crystal-form transition. The crystal plane of non-epitaxial crystals barely

https://doi.org/10.1021/acsomega.1c01365
ACS Omega 2021, 6, 11762−11771

slips when the large amount of epitaxial crystals exist in the PA66/RGO nanocomposites. RGO-adsorbing PA66 chains constrain molecule chain movement. Hence, greater size epitaxial crystals, growing on the surface of RGO, lost the crystal plane slip ability of the original PA66 α-form crystal. Moreover, non-slip epitaxial crystals greatly reduce the ability of amorphous phase and non-epitaxial crystals to respond to stress. The epitaxial crystals can constrain the deformation of amorphous phase and the crystal form transition of non-epitaxial crystals around them. The schematic diagram of structural evolution of non-epitaxial and epitaxial crystals during uniaxial deformation of PA66/RGO nanocomposites is exhibited in Figure 9. We simply assume a stretching ropes-ball process, with slipknots and dead knots, to better comprehend the structural evolution of nanocomposites during uniaxial deformation. Epitaxial crystals, non-epitaxial crystals, and nanocomposites can be assumed to be dead knot, slipknot, and ropes-ball, respectively. When a ball of ropes with only slipknots is stretched, a certain amount of slipknots have the chance to be unfastened. This process means the crystal form transition of non-epitaxial crystal during uniaxial deformation. With the increase of the amount of dead knots, fewer and fewer slipknots can be unfastened. In addition, there are a relatively large number of H-bonds in the crystals and amorphous phase of PA66. These H-bonds make the amorphous phase of PA66 rigid. From experimental results, the intuitive difference of these is the change of strain. With the addition of a minor amount of RGO, the strain obviously decreases. The RGO does not change the crystal form of PA66, but a certain amount of H-bonds are destroyed in the amorphous phase of PA66 matrix. It is the other reason for the decrease of strain.

3. CONCLUSIONS

In summary, we investigated the uniaxial deformation of the PA66/RGO nanocomposites using the *in situ* synchrotron SAXS/WAXD techniques and then analyzed the effect of interfacial epitaxial crystallization of PA66 crystallized at the surfaces of RGO. In the PA66/RGO nanocomposites, the epitaxial crystals do not display the slip of crystal plane during uniaxial deformation. The amorphous phase and non-epitaxial crystals, around the epitaxial crystals, are also constrained, so that the deformation of the amorphous phase, the rearrangement of crystallites, and the crystal-plane slip of non-epitaxial crystals become more difficult with the increase of the epitaxial crystals. Through this work, the function of epitaxial crystals is clear. Hence, this work has a special significance for the mechanical property study of polymer/inorganic nanocomposites with epitaxial crystals.

4. EXPERIMENTAL SECTION

4.1. Materials. PA66 (101L) used in this work was purchased from DuPont Ltd., (USA). Natural flake graphite with a mean particle size of 50 μm was supplied by Qingdao Jiuyi Graphite Co., Ltd. (Shandong, China)

4.2. Sample Preparation. GO was exfoliated by ultrasonication from graphite oxide, which was produced by modified Hummers' method.[53] RGO was prepared by thermal exfoliation and reduction of GO.[22]

The PA66 granules were dried in a vacuum oven at 110 °C for 12 h and then blended with RGO using a twin-screw extruder (HAAKE MiniLab II). The temperature of the twin-screw extruder was maintained at 275 °C. The screw speed was maintained 60 rpm. The PA66/RGO nanocomposites were injection-molded to get test bars (12 × 2 × 1 mm), and the temperature for injection molding was set as 150 °C for 10 min. Three different component ratios of A66 and 0.1 wt % RGO (named as PA66/RGO 0.1), 0.5 wt % RGO (named as PA66/RGO 0.5), and 1.0 wt % RGO (named as PA66/RGO 1.0) nanocomposites and a pure PA66 were prepared for stretching. This preparation method of Pure PA66 and PA66/RGO nanocomposites was the same as that used in our previous work,[20] and the RGO can be well dispersed in the PA66 matrix with such a preparation method according to the results of structural and mechanical properties.

4.3. *In Situ* SAXS and WAXS Measurement. *In situ* 2D WAXD and 2D SAXS experiments, carried out on the BL16B1 beamline in the Shanghai Synchrotron Radiation Facility (SSRF), were employed to follow the stretching process of PA66/RGO nanocomposites at room temperature. The uniaxial stretching of PA66/RGO nanocomposites, along the horizontal direction, was performed with a tensile testing device (TST350, Linkam, U.K.) with the tensile rate of 1.2 mm/min. The X-ray wavelength was 1.239 Å. The calibrated distance from the sample to detector was 128.0 mm. Moreover, the calibrated distance from the sample to detector of 2D-SAXS experiments was 5210 mm. The data of the WAXD and SAXS experiments were reduced by the program FIT2D. The 1D-WAXD curves and SAXS curves were obtained from the azimuthal integral of 2D X-ray patterns. The SAXS curves were Lorentz corrected.

AUTHOR INFORMATION

Corresponding Author

Zongbao Wang − *Ningbo Key Laboratory of Specialty Polymers, School of Materials Science and Chemical Engineering, Ningbo University, Ningbo 315211, PR China;* orcid.org/0000-0002-7399-4638; Email: wangzongbao@nbu.edu.cn

Authors

Enyi Chi − *Ningbo Key Laboratory of Specialty Polymers, School of Materials Science and Chemical Engineering, Ningbo University, Ningbo 315211, PR China;* orcid.org/0000-0002-5518-3487

Yujing Tang − *Sinopec Beijing Research Institute of Chemical Industry, Beijing 100013, People's Republic of China;* orcid.org/0000-0002-4092-8204

Complete contact information is available at: https://pubs.acs.org/10.1021/acsomega.1c01365

Notes

The authors declare no competing financial interest.

ACKNOWLEDGMENTS

This work was supported by the National Natural Science Foundation of China (51973097, 51773101). We thank SSRF for supporting the SAXS and WAXD test.

REFERENCES

(1) Gray, D. H.; Hu, S. L.; Juang, E.; Gin, D. L. Highly ordered polymer-inorganic nanocomposites via monomer self-assembly: In situ condensation approach. *Adv. Mater.* **1997**, *9*, 731−736.

(2) Rahmat, M.; Hubert, P. Carbon nanotube-polymer interactions in nanocomposites: A review. *Compos. Sci. Technol.* **2011**, *72*, 72−84.

(3) Takenaka, Y.; Miyaji, H.; Hoshino, A.; Tracz, A.; Jeszka, J. K.; Kucinska, I. Interface structure of epitaxial polyethylene crystal grown on HOPG and MoS2 substrates. *Macromolecules* **2004**, *37*, 9667−9669.
(4) Li, C. Y.; Li, L.; Cai, W.; Kodjie, S. L.; Tenneti, K. K. Nanohybrid Shish-kebabs: Periodically functionalized carbon nanotubes. *Adv. Mater.* **2005**, *17*, 1198−1202.
(5) Petermann, J.; Broza, G.; Rieck, U.; Kawaguchi, A. Epitaxial interfaces in semicrystalline polymers and their applications. *J. Mater. Sci.* **1987**, *22*, 1477−1481.
(6) Petermann, J.; Xu, Y. Mechanical-properties of epitaxially crystallized 1,4-polypropylene. *Colloid Polym. Sci.* **1991**, *269*, 455−459.
(7) Gross, B.; Peterman, J. Synergisms of mechanical-properties in blends of semi-crystalline polymers. *J. Mater. Sci.* **1984**, *19*, 105−112.
(8) Ramanathan, T.; Abdala, A. A.; Stankovich, S.; Dikin, D. A.; Herrera-Alonso, M.; Piner, R. D.; Adamson, D. H.; Schniepp, H. C.; Chen, X.; Ruoff, R. S.; Nguyen, S. T.; Aksay, I. A.; Prud'Homme, R. K.; Brinson, L. C. Functionalized graphene sheets for polymer nanocomposites. *Nat. Nanotechnol.* **2008**, *3*, 327−331.
(9) Deng, Y.; Li, Y.; Dai, J.; Lang, M.; Huang, X. An Efficient Way to Functionalize Graphene Sheets with Presynthesized Polymer via ATNRC Chemistry. *J. Polym. Sci., Polym. Chem.* **2011**, *49*, 1582−1590.
(10) Yang, B.-X.; Pramoda, K. P.; Xu, G. Q.; Goh, S. H. Mechanical reinforcement of polyethylene using polyethylene-grafted multiwalled carbon nanotubes. *Adv. Funct. Mater.* **2007**, *17*, 2062−2069.
(11) Cao, Y.; Lai, Z.; Feng, J.; Wu, P. Graphene oxide sheets covalently functionalized with block copolymers via click chemistry as reinforcing fillers. *J. Mater. Chem.* **2011**, *21*, 9271−9278.
(12) Salavagione, H. J.; Martínez, G. Importance of Covalent Linkages in the Preparation of Effective Reduced Graphene Oxide-Poly(vinyl chloride) Nanocomposites. *Macromolecules* **2011**, *44*, 2685−2692.
(13) Feng, L.; Zhou, Z.; Dufresne, A.; Huang, J.; Wei, M.; An, L. Structure and Properties of New Thermoforming Bionanocomposites Based on Chitin Whisker-Graft-Polycaprolactone. *J. Appl. Polym. Sci.* **2009**, *112*, 2830−2837.
(14) Hu, H.; Wang, X.; Wang, J.; Wan, L.; Liu, F.; Zheng, H.; Chen, R.; Xu, C. Preparation and properties of graphene nanosheets-polystyrene nanocomposites via in situ emulsion polymerization. *Chem. Phys. Lett.* **2010**, *484*, 247−253.
(15) Sun, T.; Garcés, J. M. High-performance polypropylene-clay nanocomposites by in-situ polymerization with metallocene/clay catalysts. *Adv. Mater.* **2002**, *14*, 128−130.
(16) Kim, H.-S.; Lee, B.-H.; Choi, S.-W.; Kim, S.; Kim, H.-J. The effect of types of maleic anhydride-grafted polypropylene (MAPP) on the interfacial adhesion properties of bio-flour-filled polypropylene composites. *Compos. Appl. Sci. Manuf.* **2007**, *38*, 1473−1482.
(17) Li, H.; Yan, S. Surface-Induced Polymer Crystallization and the Resultant Structures and Morphologies. *Macromolecules* **2011**, *44*, 417−428.
(18) Hu, J.; Xin, R.; Hou, C.-Y.; Yan, S.-K.; Liu, J.-C. Direct Comparison of Crystal Nucleation Activity of PCL on Patterned Substrates. *Chinese J. Plolym. Sci.* **2019**, *37*, 693−699.
(19) Ning, N.; Fu, S.; Zhang, W.; Chen, F.; Wang, K.; Deng, H.; Zhang, Q.; Fu, Q. Realizing the enhancement of interfacial interaction in semicrystalline polymer/filler composites via interfacial crystallization. *Prog. Polym. Sci.* **2012**, *37*, 1425−1455.
(20) Chi, E. Y.; An, M. F.; Yao, G. B.; Tian, F.; Wang, Z. B. The Influence of Epitaxial Crystallization on the Mechanical Properties of Polyamide 66/Reduced Graphene Oxide Nanocomposite Injection Bar. *Crystals* **2017**, *7*, 384.
(21) Wang, B.; Li, Y.; Weng, G.; Jiang, Z.; Chen, P.; Wang, Z.; Gu, Q. Reduced graphene oxide enhances the crystallization and orientation of poly(epsilon-caprolactone). *Compos. Sci. Technol.* **2014**, *96*, 63−70.
(22) Wang, B.; Zhang, Y.; Zhang, J.; Li, H.; Chen, P.; Wang, Z.; Gu, Q. Noncovalent Method for Improving the Interaction between Reduced Graphene Oxide and Poly(epsilon-caprolactone). *Ind. Eng. Chem. Fundam.* **2013**, *52*, 15824−15828.
(23) Sano, M.; Sasaki, D. Y.; Kunitake, T. Polymerization induced epitaxy scanning tunneling microscopy of a hydrogen bonded sheet of polyamide on graphite. *Science* **1992**, *258*, 441−443.
(24) Cheng, S.; Chen, X.; Hsuan, Y. G.; Li, C. Y. Reduced Graphene Oxide-Induced Polyethylene Crystallization in Solution and Nanocomposites. *Macromolecules* **2012**, *45*, 993−1000.
(25) Cartier, L.; Okihara, T.; Ikada, Y.; Tsuji, H.; Puiggali, J.; Lotz, B. Epitaxial crystallization and crystalline polymorphism of polylactides. *Polymer* **2000**, *41*, 8909−8919.
(26) Pashley, D. W. The nucleation growth strure and epitaxy of thin surface films. *Adv. Phys.* **1965**, *14*, 327−416.
(27) Li, L.; Hu, J.; Li, Y.; Huang, Q.; Sun, X.; Yan, S. Evidence for the Soft and Hard Epitaxies of Poly(L-lactic acid) on an Oriented Polyethylene Substrate and Their Dependence on the Crystallization Temperature. *Macromolecules* **2020**, *53*, 1745−1751.
(28) Guan, G.; Zhang, J.; Sun, X.; Li, H.; Yan, S.; Lotz, B. Oriented Overgrowths of Poly(l-Lactide) on Oriented Isotactic Polypropylene: A Sequence of Soft and Hard Epitaxies. *Macromol. Rapid Commun.* **2018**, *39*, 1800353.
(29) Li, L.; Xin, R.; Li, H.; Sun, X.; Ren, Z.; Huang, Q.; Yan, S. Tacticity-Dependent Epitaxial Crystallization of Poly(L-lactic acid) on an Oriented Polyethylene Substrate. *Macromolecules* **2020**, *53*, 8487−8493.
(30) Novoselov, K. S.; Geim, A. K.; Morozov, S. V.; Jiang, D.; Zhang, Y.; Dubonos, S. V.; Grigorieva, I. V.; Firsov, A. A. Electric field effect in atomically thin carbon films. *Science* **2004**, *306*, 666−669.
(31) Lee, C.; Wei, X.; Kysar, J. W.; Hone, J. Measurement of the elastic properties and intrinsic strength of monolayer graphene. *Science* **2008**, *321*, 385−388.
(32) Kuilla, T.; Bhadra, S.; Yao, D.; Kim, N. H.; Bose, S.; Lee, J. H. Recent advances in graphene based polymer composites. *Prog. Polym. Sci.* **2010**, *35*, 1350−1375.
(33) Kim, H.; Abdala, A. A.; Macosko, C. W. Graphene/Polymer Nanocomposites. *Macromolecules* **2010**, *43*, 6515−6530.
(34) Verdejo, R.; Bernal, M. M.; Romasanta, L. J.; Lopez-Manchado, M. A. Graphene filled polymer nanocomposites. *J. Mater. Chem.* **2011**, *21*, 3301−3310.
(35) Bunn, C. W.; Garner, E. V. The crystal structures of 2 polyamides (nylon). *Proc. Roy. Soc. Lond. Math. Phys. Sci.* **1947**, *189*, 39.
(36) Qin, H.; Su, Q.; Zhang, S.; Zhao, B.; Yang, M. Thermal stability and flammability of polyamide 66/montmorillonite nanocomposltes. *Polymer* **2003**, *44*, 7533−7538.
(37) Araujo, E. M.; Araujo, K. D.; Paz, R. A.; Gouveia, T. R.; Barbosa, R.; Ito, E. N. Polyamide 66/Brazilian Clay Nanocomposites. *J. Nanomater.* **2009**, *2009*, 136856.
(38) Song, L.; Hu, Y.; He, Q. L.; You, F. Study on Crystallization, Thermal and Flame Retardant Properties of Nylon 66/Organoclay Nanocomposites by in situ Polymerization. *J. Fire Sci.* **2008**, *26*, 475−492.
(39) Trifan, D. S.; Terenzi, J. F. Extents of hydrogen bonding in polyamides and polyurethanes. *J. Polym. Sci.* **1958**, *28*, 443−445.
(40) Garcia, D.; Starkweather, H. W. Hydrogen bonding in nylon-66 and model compounds. *J. Polym. Sci., Polym. Phys.* **1985**, *23*, 537−555.
(41) Coleman, M. M.; LEE, K. H.; SKROVANEK, D. J.; PAINTER, P. C. Hydrogen bonding in polymers. 4. infrared temperature studies of a simple. *Macromolecules* **1986**, *19*, 2149−2157.
(42) Kinoshita, Y. An investigation of the structures of polyamide series. *Makromol. Chem.* **1959**, *33*, 1−20.
(43) Meyer, J. C.; Geim, A. K.; Katsnelson, M. I.; Novoselov, K. S.; Booth, T. J.; Roth, S. The structure of suspended graphene sheets. *Nature* **2007**, *446*, 60−63.
(44) Arimoto, H.; Ishibashi, M.; Hirai, M.; Chatani, Y. Structure of the α-Form of Nylon 6. *Polym. Sci.* **1965**, *3*, 317−326.
(45) Wittmann, J. C.; Lotz, B. Epitaxial crystallization of polymers on organic and polymeric substrates. *Prog. Polym. Sci.* **1990**, *15*, 909−948.

https://doi.org/10.1021/acsomega.1c01365
ACS Omega 2021, 6, 11762−11771

(46) Hughes, D. J.; Mahendrasingam, A.; Heeley, E. L.; Oatway, W. B.; Martin, C.; Towns-Andrews, E.; Fuller, W. Time-Resolved Simultaneous SAXS/WAXS of the Drawing of Polyethylene at the Daresbury SRS. *J. Synchrotron Radiat.* **1996**, *3*, 84−90.
(47) Jiang, Z.; Tang, Y.; Men, Y.; Enderle, H.-F.; Lilge, D.; Roth, S. V.; Gehrke, R.; Rieger, J. Structural Evolution of Tensile-Deformed High-Density Polyethylene during Annealing: Scanning Synchrotron Small-Angle X-ray Scattering Study. *Macromolecules* **2007**, *40*, 7263−7269.
(48) Wang, L.; Dong, X.; Huang, M.; Wang, D. Transient microstructure in long alkane segment polyamide: Deformation mechanism and its temperature dependence. *Polymer* **2016**, *97*, 217−225.
(49) Toki, S.; Sics, I.; Ran, S.; Liu, L.; Hsiao, B. S.; Murakami, S.; Senoo, K.; Kohjiya, S. New insights into structural development in natural rubber during uniaxial deformation by in situ synchrotron X-ray diffraction. *Macromolecules* **2002**, *35*, 6578−6584.
(50) Oono, R.; Miyasaka, K.; Ishikawa, K. Crystallization kinetics of blaxlally stretched natural-rubber. *J. Polym. Sci., Polym. Phys.* **1973**, *11*, 1477−1488.
(51) Wang, Z.; An, M.; Xu, H.; Lv, Y.; Tian, F.; Gu, Q. Structural evolution from shish-kebab to fibrillar crystals during hot-stretching process of gel spinning ultra-high molecular weight polyethylene fibers obtained from low concentration solution. *Polymer* **2017**, *120*, 244−254.
(52) An, M.; Xu, H.; Lv, Y.; Gu, Q.; Tian, F.; Wang, Z. An in situ small-angle X-ray scattering study of the structural effects of temperature and draw ratio of the hot-drawing process on ultra-high molecular weight polyethylene fibers. *RSC Adv.* **2016**, *6*, 51125−51134.
(53) Kim, J.-J.; JANG, T.-S.; KWON, Y.-D.; KIM, U. Y.; KIM, S. S. Structural Study of microporous polypropylene hollow-fiber membranes made by the melt-spinning and cold-stretching method. *J. Membr. Sci.* **1994**, *93*, 209−215.
(54) Duan, T.; Xu, H.; Tang, Y.; Jin, J.; Wang, Z. Effect of epitaxial crystallization on the structural evolution of PCL/RGO nanocomposites during stretching by in-situ synchrotron radiation. *Polymer* **2018**, *159*, 106−115.
(55) Li, Y. G.; Duan, T. C.; Yao, G. B.; Tang, Y. J.; Miao, W. J.; Wang, Z. B. Structural evolution of stretch deformed HDPE/RGO nanocomposites: An in-situ synchrotron SAXS and WAXD study. *Compos. Sci. Technol.* **2019**, *183*, 107798.

https://doi.org/10.1021/acsomega.1c01365
ACS Omega 2021, 6, 11762−11771